Supplementary Materials:

Arbitrary Eigenmode Reshaping Induced by Distributed Non-Reciprocity in Non-Hermitian Systems

Zhaomin Rong[1†], Yu Chen[2†], Yanan Bai[1], Tie Jun Cui[2*], Lei Zhou[3,4,5*],
Shuo Liu[2*], Shaojie Ma[1,3,5*]

[1]College of Future Information Technology, Fudan University, Shanghai 200433, China

[2]State Key Laboratory of Millimeter Waves, Southeast University, Nanjing 210096, China

[3]Shanghai Key Laboratory of Metasurfaces for Light Manipulation, Shanghai 200433, China

[4]State Key Laboratory of Surface Physics and Department of Physics, Fudan University, Shanghai 200433, China

[5]Key Laboratory of Micro and Nano Photonic Structures (MOE), Fudan University, Shanghai 200433, China

[*]Correspondence: tjcui@seu.edu.cn (T.J.C.); phzhou@fudan.edu.cn (L.Z.);
liushuo.china@seu.edu.cn (S.L.); and shaojiema@fudan.edu.cn (S.M.)

[†]These authors contributed equally to this work.

Contents

I. Theoretical Analysis

1.1 1D nearest-neighbor TBM model

To demonstrate the ubiquity of the non-Hermitian reshaping effect, we investigate a 1D non-reciprocal nearest-neighbor Tight-Binding Model (TBM). This model elucidates the transition behavior of electrons within a 1D non-reciprocal atomic chain. By considering only nearest-neighbor interactions and neglecting the electron-electron coupling, the electron dynamics can be described using a single-particle Hamiltonian.

$$\hat{H} = \sum_{n=1}^{N} w_n^{(1)} |n+1\rangle\langle n| + w_n^{(2)} |n\rangle\langle n+1| + l_n |n\rangle\langle n| \qquad (S1)$$

Here, $|n\rangle$ represents the quantum states where an electron is located on the n-th unit cell. Such atomic chain comprises N unit cells, and the flexibility of this model manifests in the parameter $w_n^{(1)}$ and $w_n^{(2)}$, where the non-reciprocal transition coefficients between each pair of atoms can be entirely inhomogeneous and arbitrary.

By introducing non-reciprocity into the hopping coefficients through $w_n^{(1)} \neq \mathrm{conj}\left(w_n^{(2)}\right)$, a non-Hermitian TBM model can be constructed. A common definition sets the hopping coefficient $w_n^{(1)} = w_n + \delta$ in one direction while setting the other $w_n^{(2)} = w_n$. In this article, we modify the hopping coefficient to the right as $w_n^{(1)} = w_n \cdot e^{\kappa_n}$ and to the left as $w_n^{(2)} = w_n \cdot e^{-\kappa_n}$. These two formulations are mathematically equivalent when $w_n^{(2)} = w_n \cdot e^{-\kappa_n}$. The item κ_n is used to characterize the distribution of arbitrary non-reciprocity in the system.

$$\begin{aligned} \mathbf{H} &= \sum_{m,n} H_{NR,mn} \cdot |m\rangle\langle n| \\ &= \sum_{n} w_n \left(e^{-\kappa_n - i\phi_n} |n\rangle\langle n+1| + e^{\kappa_n + i\phi_n} |n+1\rangle\langle n|\right) + l_n |n\rangle\langle n| \end{aligned} \qquad (S2)$$

For the special case of $N = 4$, the Hamiltonian of such a non-Hermitian model can be expressed as:

$$H_{NR} = \begin{pmatrix} l_1 & w_1 e^{-\kappa_1} & 0 & 0 \\ w_1 e^{-\kappa_1} & l_2 & w_2 e^{-\kappa_2} & 0 \\ 0 & w_2 e^{-\kappa_2} & l_3 & w_3 e^{-\kappa_3} \\ 0 & 0 & w_3 e^{-\kappa_3} & l_4 \end{pmatrix} \qquad (S3)$$

The eigenvalues of the Hamiltonian can be obtained by solving the characteristic equation $|H - E \cdot I| = 0$, where I is the identity matrix. The matrix associated with this determinant is known as a nth-order *tridiagonal matrix* in mathematics:

$$f_n = \begin{vmatrix} a_1 & b_1 & & & \\ c_1 & a_2 & \ddots & & \\ & \ddots & \ddots & \ddots & \\ & & \ddots & a_{n-1} & b_{n-1} \\ & & & c_{n-1} & a_n \end{vmatrix} \qquad (S4)$$

which possesses several interesting properties that can simplify the calculation of eigenvalues. It is revealed that b_n and c_n never appear separately in this determinant and they always emerge in pairs as products.

Proof

Assuming that neither $|H_{n-1} - EI_{n-1}|$ nor $|H_{n-2} - EI_{n-2}|$ contains terms involving κ. From Eq. S5, it follows that:

$$|H_n - EI_n| = (a_{n-1} - E) \cdot |H_{n-1} - EI_{n-1}| - b_{n-1}c_{n-1} \cdot |H_{n-2} - EI_{n-2}|,$$

where $b_{n-1} = w_{n-1}e^{\kappa_{n-1}}$, $c_{n-1} = w_{n-1}e^{-\kappa_{n-1}}$, giving $b_{n-1} \cdot c_{n-1} = w_{n-1}^2$. Since b_{n-1} and c_{n-1} always appears as a product, the dependence on κ_n is exactly eliminated.

As the induction bases, we note that

$$|H_2 - EI_2| = E^2 - w_1^2$$

$$|H_3 - EI_3| = -E^3 + Ew_1^2 + Ew_2^2$$

neither of which contains terms associated with κ_n. Consequently, by induction, $|H_n - EI_n|$ is independent of κ for any tridiagonal matrix H_n.

The sequence f_n satisfies the recurrence relation:

$$f_n = a_n f_{n-1} - c_{n-1} b_{n-1} f_{n-2} \tag{S5}$$

The subscript indicates the order of the tridiagonal matrix. It can be mathematically proved that $|H - E \cdot I|$ does not contain any terms related to κ.

Thus, this non-Hermitian Hamiltonian can be related to the Hermitian Hamiltonian through a similarity transformation, and the relation can always be expressed as:

$$H_{NR} = T H_R T^{-1} \tag{S6}$$

where T represents the similarity transformation matrix. In the nearest-neighbor TBM model discussed earlier, T can be a diagonal matrix $\hat{T} = \mathrm{diag}(t_1, t_2, \cdots)$ and $H_{NR,mn} = t_m{}^{-1} t_n H_{R,mn}$, where H_{mn} is nonzero only when $m = n \pm 1$. The spatial distributed non-reciprocity κ_n is directly related to the recursive relation for t_n:

$$t_{n+1} = e^{\kappa_n} \cdot t_n \tag{S7}$$

This recursive relation completely determines the expression of the diagonal similarity matrix T. Such a similarity transformation can be used to modify the eigenfunctions. As a result, regardless of the choice of spatial function of the non-Hermitian coefficients κ_n, we can achieve precise theoretical predictions of the modified eigenfunctions. This undoubtedly paves the way for new possibilities in non-Hermitian modulation.

1.2 General TBM models

In the above derivation, we have relied on the mathematical properties of tridiagonal matrices. However, the Hamiltonian matrix is generally not tridiagonal. This implies that our derivation cannot be directly extended to cases involving next-nearest-neighbor interactions or higher dimensions.

Nevertheless, some aspects of the above results still hold in more general cases. While we can **NOT** guarantee that an arbitrary non-Hermitian Hamiltonian can always be transformed into a Hermitian one with well-defined dispersion spectrum and topological property through the similarity transformation (this conclusion is inevitable; otherwise, no new physics would emerge from non-Hermitian systems), it is still possible to apply a diagonal similarity transformation T to a well-defined system H_R. This Hamiltonian H_R is not restricted to a Hermitian one but can be any TBM model with known properties. Consequently, a corresponding non-reciprocal Hamiltonian $H_{NR} = T^{-1} H_R T$ can be constructed, which inherits the dispersion spectrum and topological properties of the base Hamiltonian H_R, while offering arbitrarily adjustable mode distribution. These features can be effectively applied to specific mode control applications, such as the design of laser cavities.

II. Numerical Verifications

2.1 1D NH-SSH model

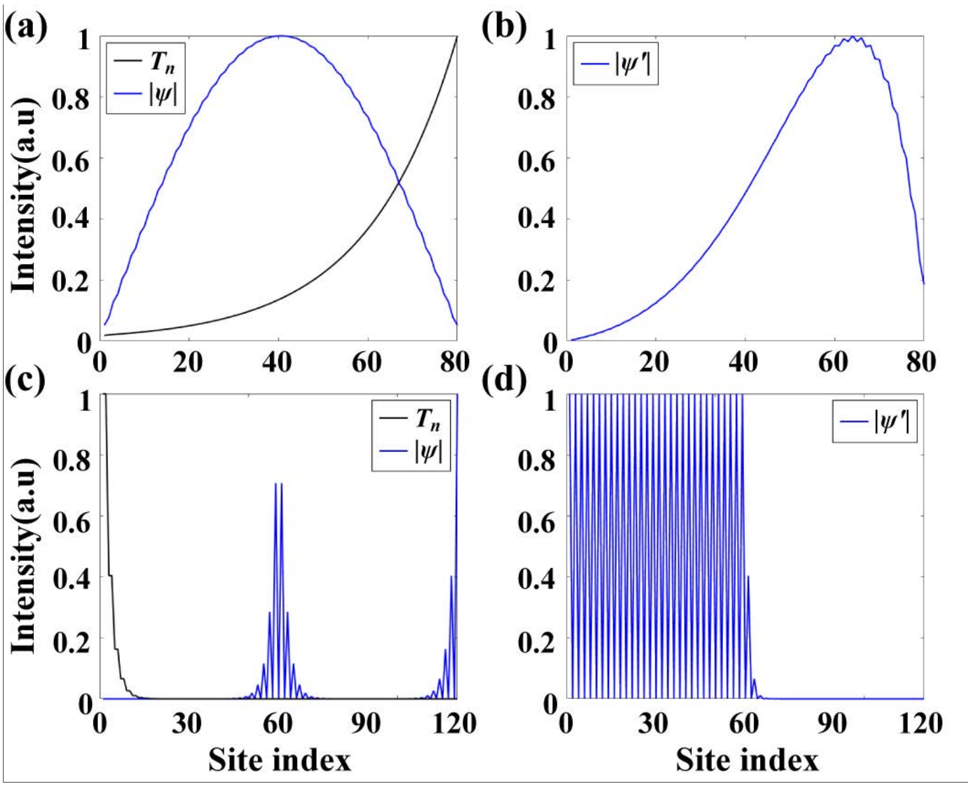

Fig. S1. Illustration of two typical models of NHRE. (a-b) Schematic diagram of the non-Hermitian skin effect, where the blue solid line in (a) represents a representative bulk state of the corresponding Hermitian SSH model, and the black solid line denotes the envelope function t_n. The product of these two functions results in the solid line in (b), which signifies the bulk states of the non-Hermitian SSH model. (c-d) Schematic diagram of the non-Hermitian morphing effect, where the blue solid line in (c) depicts the edge states at the domain wall, and the black solid line again represents the envelope function t_n. Their product yields the blue solid line in (d), corresponding to the propagable topological zero mode.

The theoretical analysis yielded promising results, demonstrating that non-Hermitian manipulations can be applied to arbitrary models while preserving their topological properties. In the following numerical calculations, we will validate these theoretical findings using the non-Hermitian SSH model and explore the intriguing aspects of this manipulation approach.

Here, we consider two typical models. When taking $\kappa = \kappa_0$ and setting $[w_{2i}, w_{2i+1}]$ to $[w, v]$, this scenario corresponds to the well-known non-Hermitian skin effect (NHSE). Therefore, T can be solved as $t_n = C \cdot \exp(\kappa_0 n)$, which directly leads to the non-Hermitian skin effect, as shown in Fig. S1(a-b). Furthermore, from the corresponding Hermitian Hamiltonian, it is evident that the topological transition point occurs at $v = w$, consistent with the result obtained from the generalized Brillouin zone theory.

In the second model, we choose $\kappa_n = -\kappa_0 \cdot \Theta(n_0 - n)$ as a step function, with the non-Hermitian modulation applied only to the region where $n \leqslant n_0$. Therefore, T can be expressed as $t_n = \exp[-\kappa_0 (n - n_0)]$ when $n \leqslant n_0$ and $t_n = 1$ when $n > n_0$. Preview article [37] combined two SSH models with different topological characteristics to induce edge states at the domain wall, where the index n_0 denotes the interface separating the two model. These edge states can be represented by $\psi(n) = C' \exp[\sigma \cdot (n - n_0)]$ when $n \leqslant n_0$, where σ denotes the decay rate of the edge state. When the parameters are appropriately chosen, the envelope function t_n applied to the edge states precisely counteracts the mode decay and yields a constant field distribution. This is fully consistent with the conclusions of the preview article on the non-Hermitian morphing effect, as shown in Fig. S1(c-d).

A slightly more complex scenario than a piecewise κ is when $\kappa(n)$ is linearly distributed, i.e. $\kappa_n = -\alpha \cdot (n - r)$, where α and r are modulation parameters. According to Eq. S7, we can derive the expression for t_n in this case:

$$t_n = C \exp\left[-\frac{1}{2}\alpha (n - n_c)^2\right] \qquad (S8)$$

Here, $n_c = r - 3/2$ represents the central position of the modulated function, and C is a constant generated during the calculation that is not of concern. If α is positive, the envelope function t_n essentially becomes a Gaussian function.

Assuming the expression for the edge state satisfies $\psi(n) = A\exp(-\sigma n)$, where σ represents the decay rate of the edge state. According to Eq. S7, multiplying t_n by the edge state wave function yields

$$\psi(n) = C'\exp\left[\kappa_0\left(n - n_c - \frac{\sigma}{2\kappa_0}\right)^2\right] \qquad (S9)$$

This is the analytical expression for the modulated wave function, indicating that the edge state is modulated into a Gaussian function and translated by a certain distance, shifting from the boundary into the bulk, as shown in Fig. 1(e).

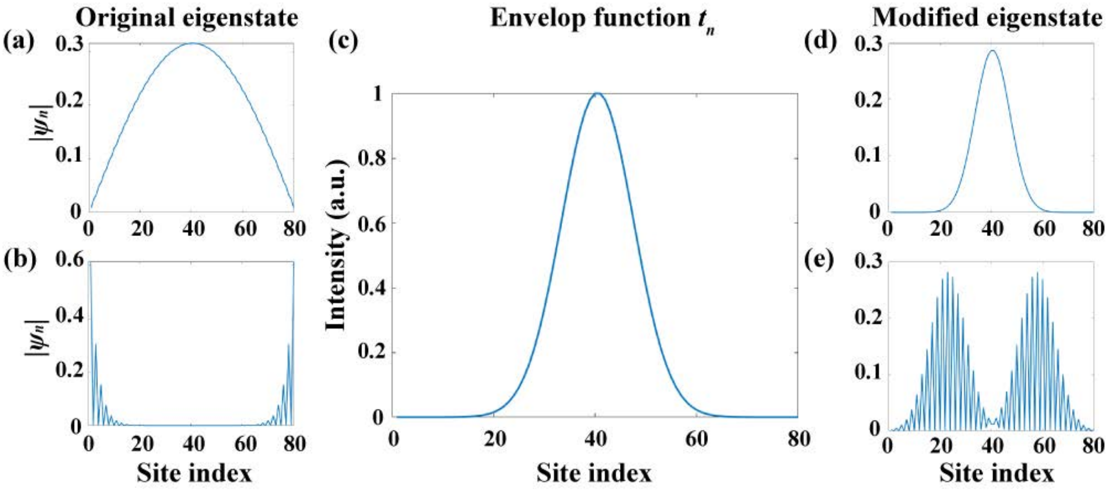

Fig. S2. Manipulation of bulk and edge states via NHRE. (a-b) Spatial distribution of the original (a) bulk state and (b) edge state, respectively. (c) Envelope function t_n. (d-e) Spatial distribution of the modified (d) bulk state and (e) edge state, respectively.

Figure S2 illustrates the manipulation of bulk and edge states, respectively. Both the bulk states in Fig. S2(a) and edge states in Fig. S2(b) are shifted towards the center under the influence of the Gaussian shaped envelope function t_n depicted in Fig. S2(c).

Notably, the positions of the modulated edge state in Fig. S2(d) are not fully correlated with the bulk state in Fig. S2(e). The bulk states are confined to the center while the edge states can still be shifted to any desired position, under fine-tuning of the system parameters. This indicates that, although NHRE acts on all modes simultaneously, we can still achieve relatively independent control over different types of modes. This further enhances the tunability of NHRE.

2.2 2D NH-BBH model

While our previous calculations validated the framework in 1D, we now apply it to the 2D BBH model to demonstrate its broader applicability to more general systems. The most notable feature of the BBH model is the corner-localized modes that emerge within the bandgap. We define the field distribution of the corner state as $\psi(n)$, and the target wavefunction as $\psi'(n)$. Consequently, the envelope function t_n can be expressed as $t_n = \psi'(n)/\psi(n)$. This similarity transformation introduces a non-Hermitian modulation to all Hamiltonian elements connected to site n. As the modulation simply rescales the original Hermitian couplings, the tight-binding connectivity is preserved while the coupling strengths are modified. In the BBH model, the resulting Hamiltonian thus retains only nearest-neighbor interactions, but with almost all couplings rendered nonreciprocal.

This regulation allows for arbitrary control over a specific state. In the main text, we numerically demonstrated arbitrary manipulation of the field distribution of a corner state, localizing the field at another corner, two corners, the center, or any desired field configuration.

III. Topological Circuit Verification

3.1 Generation of Non-Reciprocity in Circuit Systems

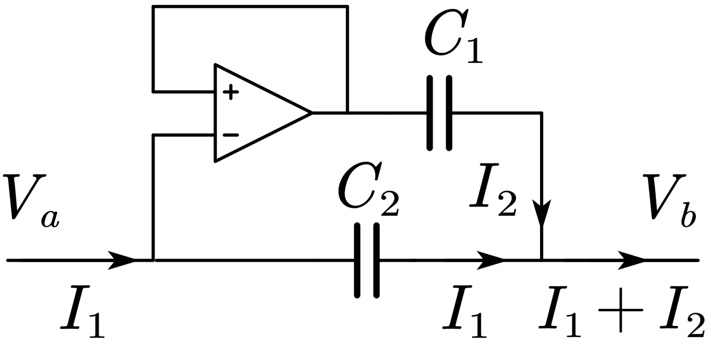

Fig. S3. Generation of nonreciprocity in circuit system.

Non-reciprocal coupling in the topological circuit is realized via unidirectional coupling capacitors. As depicted in Fig. S3, each coupler comprises a voltage follower in series with one coupling capacitor, placed in parallel with another coupling capacitor. The voltage follower is implemented via an operational amplifier (Op-Amp) configured with negative feedback. Exploiting the virtual short and virtual open circuit conditions at the Op-Amp's input terminals, the left-side current path through the capacitor is blocked, while the right-side path remains conductive, as shown in Fig. S3. This asymmetry produces different effective conductance, $J_{ab} = I_1/(V_b - V_a)$ and $J_{ba} = -(I_1 + I_2)/(V_a - V_b)$, between the connected nodes, thereby establishing non-reciprocal behavior.

3.2 Non-Hermitian Model Analysis via Impedance Measurements

For Hermitian topological circuits, the eigenstates can be directly extracted from self-impedance measurements. The circuit Laplacian J is generally expressed as:

$$J(w) = i\omega C \cdot H_R + \left(i\omega C_t + \frac{1}{i\omega L_t}\right) I = i\omega C \cdot [H_R - \lambda(\omega) I] \qquad (S10)$$

Here, H_R is the effective Hamiltonian of the implemented Hermitian SSH model circuit. C and C_t are the Laplacians corresponding to the coupling capacitor and the node resonance capacitor, respectively. Given that H_R is Hermitian, it is diagonalizable by a unitary matrix Ψ composed of all its orthonormal eigenstates:

$$J(w) = iwC \cdot [\Psi D \Psi^{\dagger} - \lambda(w)\Psi\Psi^{\dagger}] = iwC \cdot \Psi[D - \lambda(w)]\Psi^{\dagger} \qquad (S11)$$

Here, D is a diagonal matrix containing all the eigenvalues of H_R. Consequently, the impedance matrix Z, being the inverse of the admittance, takes the form:

$$Z(w) = [J(\omega)]^{-1} = \frac{1}{iwC} \cdot \Psi[D - \lambda(\omega)I]^{-1}\Psi^{\dagger} \qquad (S12)$$

Denoting E_n the n-th eigenstate of Hamiltonian H_R, the self-impedance Z_{aa} at node a is therefore analytically given by:

$$Z_{aa} = [J^{-1}(\omega)]_{aa} = \frac{1}{i\omega C} \cdot \sum_n \frac{|\Psi_{an}|^2}{E_n - \lambda(\omega)} \qquad (S13)$$

Analysis of Eq. S13 reveals that a resonance peak in Z_{aa} arises when the value $\lambda(w)$ matches a typical eigenvalue E_n of the Hamiltonian H_R, as the denominator approaches zero (remaining finite experimentally due to inherent resistance). This peak signifies the excitation of the n-th mode. By scanning frequency and measuring self-impedance at each circuit node, one directly maps the squared modulus of the eigenstates $|\Psi_{an}|^2$ for each mode n.

Within the non-Hermitian framework considered here, Hermitian and non-Hermitian Hamiltonians are mathematically connected via a similarity transformation, and their modes can be obtained through the transformation:

$$H_{NR} = TH_RT^{-1} = T\Psi \cdot D \cdot \Psi^{\dagger}T^{-1} \qquad (S14)$$

Substituting this expression into Eq. S11 yields

$$J(\omega) = i\omega C \cdot T\Psi \cdot [D - \lambda(\omega)] \cdot \Psi^{\dagger}T^{-1} \qquad (S15)$$

Consequently, the self-impedance Z_{aa} for this non-Hermitian system is obtained as:

$$Z_{aa} = [J^{-1}(\omega)]_{aa} = \frac{1}{i\omega C} \cdot \sum_n \left(\frac{t_a\Psi_{an} \cdot \Psi^{\dagger}_{na}t_a^{-1}}{E_n - \lambda(\omega)} \right) = \frac{1}{i\omega C} \cdot \sum_n \frac{|\Psi_{an}|^2}{E_n - \lambda(\omega)} \qquad (S16)$$

Crucially, for non-Hermitian models defined in this manner, self-impedance measurements reproduce the eigenstates of the corresponding Hermitian model, rather than the true eigenmodes of the non-Hermitian system, as shown in Fig. S4.

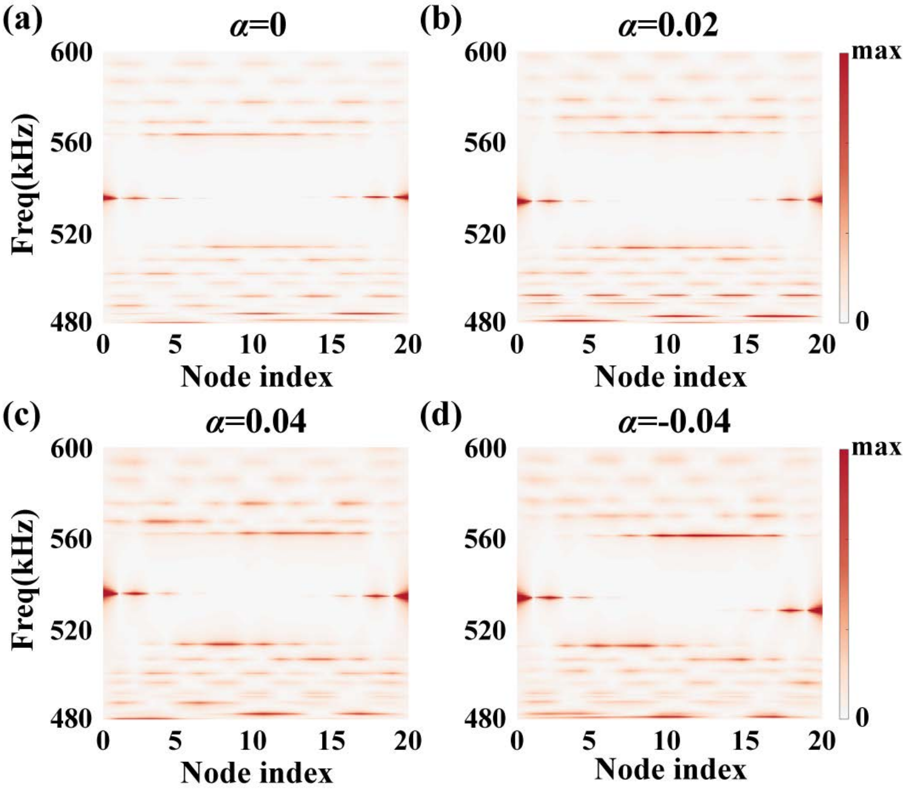

Fig. S4. Measured Z_{aa} of the topological circuit at (a) $\alpha = 0$, (b) $\alpha = 0.02$, (c) $\alpha = 0.04$ and (d) $\alpha = -0.04$. The eigenstates remain delocalized in the non-Hermitian case, just as in the Hermitian scenario.

To probe the intrinsic non-Hermitian properties, we employ the mutual impedance Z_{ab}. Similar to Eq. S16, Z_{ab} can be analytically expressed as:

$$Z_{ab} = \frac{1}{i\omega C} \cdot \sum_{n} \frac{t_a \Psi_{an} \cdot \Psi_{bn}^{*} t_b^{-1}}{E_n - \lambda(\omega)} \qquad (S17)$$

Similarly, the denominator $E_n - \lambda(\omega)$ produces a resonance peak when $E_n \approx \lambda(\omega)$. In the ideal model without parasitic resistance, the resonance peaks would diverge. To prevent numerical divergence, we manually introduce an additional imaginary component into $\lambda(\omega)$, i.e., $\tilde{\lambda}(\omega) = \lambda(\omega) - i\eta$, with η a positive infinitesimal. At $E_n = \lambda(\omega_n)$, the summation is dominated by the n-th mode, resulting in:

$$[Z(\omega_n)]_{ab} = \left(-\frac{\Psi_{bn}^{*} t_b^{-1}}{\eta\omega_n C}\right)\cdot t_a\Psi_{an} \qquad (S18)$$

Here, $\Psi_{an}' = t_a\Psi_{an}$ represents exactly the eigenstate of the non-Hermitian Hamiltonian H_{NR}, with a normalization factor depending on the excitation position b. By fixing b (e.g., $b = 1$) and scanning position a, the spatial profile of the eigenstate Ψ_{an}' can be reconstructed.

Importantly, the normalization factor depends on the choice of excitation site b through the eigenstate component Ψ_{bn}^*. Consequently, while the resonant frequency, i.e., E_n, remains unchanged for different choice of b, the relative intensity distribution across different modes varies, as shown in Fig. S5. To minimize the dependence of the spectral profile on the specific choice of b, we summed the mutual impedance and defined $\widetilde{Z}_a$ as $\widetilde{Z}_a = \Sigma_b|Z_{ab}|$ over multiple excitation positions b to characterize the circuit's spatial and frequency response. The $\widetilde{Z}_a$ spectrum reveals all mode frequencies and spatial profiles with nearly uniform intensity, as shown in Fig. S5(d).

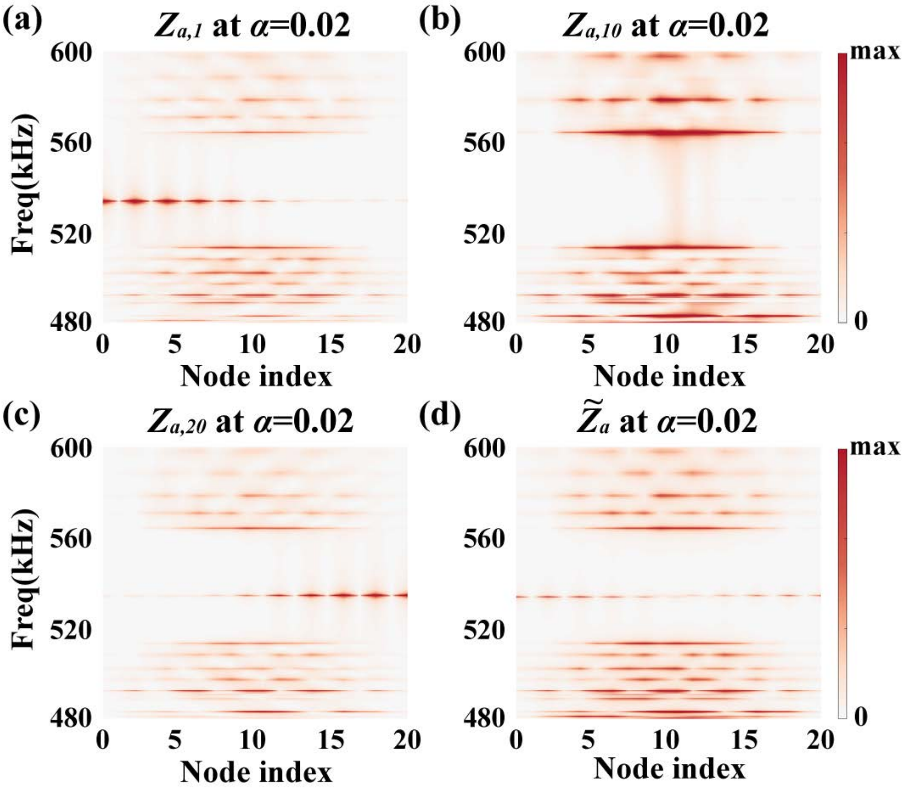

Fig. S5. Measured mutual impedance spectra of the non-Hermitian topological circuit at α = 0.02 for different excitation sites b: (a) $b = 1$, (b) $b = 10$, (c) $b = 20$, (d) summed over all b.

3.3 Data Processing: Impedance Correction

To clearly identify the modulation effect in our NHRE experiment, we deliberately selected a large value for α. This results in a large ratio of the coupling capacitance C to the resonance capacitance C_t at each node. Consequently, the resonant frequencies are restricted to a very narrow frequency band. Therefore, the loss-induced broadening of the impedance peaks results in significant spectral overlap among the bulk modes, making them indistinguishable in the measured $\tilde{Z}_a$ spectrum.

Here, we introduce a method to recover the original system information and resolve spectral overlap, even when bulk states merge due to low Q-factors. Although resistances are present in inductors, capacitors, and interconnects, parasitic inductor resistance dominates, as confirmed by individual-component measurements. Our compensation strategy therefore primarily focuses on mitigating these inductor losses.

The ideal admittance matrix, also known as circuit Laplacian, is defined by Eq. S10. The incorporation of resistive effects modifies this expression as follows:

$$J(\omega) = i\omega C \cdot H_{NR} + \left(i\omega C_t + \frac{1}{i\omega L_t + R_t}\right) \cdot I = i\omega C \cdot [H_{NR} - \lambda'(\omega) \cdot I] \qquad (S19)$$

where the resonance frequency scale item $\lambda'(w)$ becomes $\lambda'(\omega) = -C_t/C + 1/[(\omega L_t - iR_t)\omega L]$, which is complex due to the parasitic inductor resistance R_t. Therefore, the mutual impedance Z_{ab} can be analytically derived:

$$Z_{ab} = \frac{1}{i\omega C} \cdot \sum_n \left(\frac{\Psi_{nb}^{\dagger} {t_b}^{-1}}{E_n - \mathrm{Re}[\lambda(\omega)] - i\,\mathrm{Im}[\lambda(\omega)]} \right) \cdot {\Psi_{an}}' \qquad (S20)$$

This parasitic resistance broadens Z_{ab} spectrum into Lorentzian lineshapes. While moderate loss is necessary for practical observation (avoiding delta-function singularities), excessive loss leads to mode aliasing, making individual modes indistinguishable in experiments.

Now that the specific form of loss contribution in the admittance matrix is fully characterized, it can be computationally removed. This approach is conceptually analogous to the complex frequency excitation used in recent works to compensate for material loss, but is implemented here through a customized procedure.

In our experiment, mutual impedance spectrum was measured via transmission coefficient S_{21} across all nodes using a vector network analyzer (VNA). The corresponding admittance matrix was subsequently derived from the measured S-matrix:

$$J = {z_0}^{-1} \cdot (I - S) \cdot (I + S)^{-1} \qquad (S21)$$

The desired impedance matrix Z is then obtained by inverting the admittance matrix. To account for and remove the influence of inherent losses, we numerically subtracted the loss contribution using the expression:

$$J(w) = {z_0}^{-1} \cdot [I - S(\omega)] \cdot [I + S(\omega)]^{-1} + \mathrm{diag}[J_C(n, \omega)] \qquad (S22)$$

where $J_C(n, w)$ represents the loss compensation matrix, which is applied to account for and subtract experimental losses from the measured data.

In principle, the compensation strategy employs a uniform gain J_C across the entire system, which is theoretically derivable from a fixed resistance parameter:

$$J_C = \left(-\frac{1}{i\omega L_t + R_C} + \frac{1}{i\omega L_t}\right) \cdot I = \frac{R_C}{i\omega L_t (i\omega L_t + R_C)} \cdot I \qquad (S23)$$

Here, R_C serves as an approximation to the actual parasitic resistance R_t in the circuit. However, this approach yields suboptimal performance due to the intrinsic spatial non-uniformity of losses, applying a single compensation value leads inevitably to over-correction at some nodes and under-correction at others. Moreover, R_t itself exhibits strong frequency dependance, varying significantly across both high and low frequencies. Relying on a constant formula of J_C for compensation is therefore fundamentally limited. Furthermore, since J_C is typically chosen arbitrarily, the compensation process introduces a degree of subjectivity, which undermines the reproducibility of the results.

To address these issues, we propose an experimental calibration protocol based on the measured diagonal elements J_{nn} of the impedance matrix. Since these elements are theoretically lossless, we introduce a compensating resistance $J_C(n, \omega)$ to cancel out their real parts, retaining only the imaginary components. The value of $J(n,\omega)$ is determined directly from experimental data, thereby eliminating any arbitrary choices in the data processing procedure. Moreover, the resistance value autonomously self-adjusts according to both frequency and spatial position, as governed by the intrinsic response of the circuit system. Crucially, it inherently accounts for losses from all possible sources within the entire circuit—rather than being restricted only to parasitic resistance in inductive components, as is used in simplified models. This adaptive compensation effectively suppresses additional errors that would arise from idealized theoretical models.

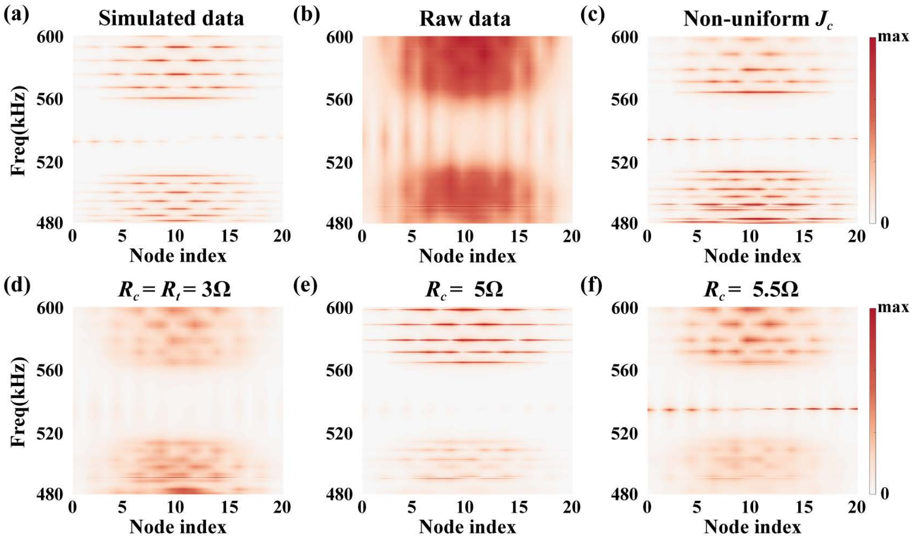

Fig. S6. Comparison of two compensation methods for the $\widetilde{Z}_a$ spectra in the non-Hermitian topological circuit. (a) Simulated data. (b) Raw experimental data. (c) Experimental data compensated via non-uniform $J_c(n,\omega)$, determined from the real part of J_{nn}. (d-f) Experimental data compensated via uniform J_c to account for the parasitic inductor resistance, with trial values: (d) R_c = 3 Ω, (e) R_c = 5 Ω, and (f) R_c = 5.5 Ω. The measured inductor resistance for a single loop is approximately $R_t \approx 3$ Ω.

A comparison of different processing methods is presented in Fig. S6. It can be observed that the calibration scheme based on J_{nn} reproduces the theoretical results with excellent agreement, yielding a clear spectral profile while eliminating any arbitrariness in the numerical processing.

IV. Non-Hermitian Modulated CROWs

A single optical ring resonant supports two degenerate whispering-gallery modes at the $n-th$ characteristic frequency ω_n: the clockwise (CW) and counterclockwise (CCW) modes, whose field profiles take the form $E \cdot exp(ik_n\theta)$ and $E \cdot exp(-ik_n\theta)$, respectively. For computational efficiency, we model the structure using a two-dimensional full-wave simulation.

In the Hermitian case, the coupled resonant optical waveguides (CROWs) are formed by linking adjacent ring resonators through a link ring, which couples modes of the same spin (CW or CCW) between neighboring sites. This coupled system still supports two degenerate modes, the CW and CCW modes. To avoid spectral overlap and suppress CW–CCW conversion, the link ring is deliberately designed with a different eigenfrequency. By tuning its radius, the link ring's resonance is shifted outside the operational band, ensuring that its own mode does not interfere with the CROW dynamics.

To introduce non-reciprocity, gain and loss are incorporated into different sections of the link ring, with the upper segment serving as the gain region and the lower segment as the loss region, as shown in Fig. S7(a). For a CW mode propagating from left to right, the field always passes through the loss section of the link ring, resulting in a reduced coupling strength to the next resonator. Conversely, when propagating from right to left, the field traverses the gain region, leading to an enhanced coupling strength. Consequently, the CW mode inside the site rings experiences direction-dependent coupling strengths, establishing a non-reciprocal interaction. It's worth noting that the CCW mode exhibits the same behavior, but with the roles of gain and loss reversed. For these two modes, the system forms two separate single-chain SSH models with opposite non-reciprocal interactions, as illustrated in Fig. S7(b). Two degenerate eigenvalues at each frequency correspond to the CW and CCW eigenstates, respectively.

However, the gain and loss in the link ring slightly modify the material impedance, inducing a small amount of reflections from CW to CCW at the interface, thereby generating coupling between the two modes. Under weak non-Hermitian modulation, this coupling is negligible. However, when the gain and loss become sufficiently strong, a small coupling emerges, lifting the degeneracy and modifying the system's eigenstate properties. Consequently, the two modes are mixed in the resulting eigenstates. This interaction can be modelled by a two-chain non-Hermitian SSH model, where each site features an additional coupling $t_{\perp}$ between the CW and CCW modes, as illustrated in Fig. 7(c). Once the weak coupling is introduced, the degeneracy is gradually lifted, altering the characteristics of the modes.

In Figs. S7(d–f), we show the energy spectra from both full-wave simulations and the uncoupled/coupled two-chain SSH TBMs. The coupled TBMs reproduce the exact level-splitting behavior observed in the simulations, with slight shifts in eigenfrequencies relative to the Hermitian Hamiltonian. These shifts vanish completely when $t_{\perp}$ is reset to zero, confirming that the source of the discrepancy with NHRE predictions lies in this offset.

Nevertheless, even with such shifts, NHRE remains valid. To illustrate this, we show the mode corresponding to the smallest eigenvalue and project it onto the CW and CCW field profiles, $E \cdot e\text{xp}(\pm i k_n \theta)$, to resolve the spatial distributions of the CW and CCW components separately, as shown in Figs. S7(g–i). The results demonstrate excellent agreement between simulation and the coupled TBMs. Despite the mode coupling, NHRE still modulates the CW component toward the center while the CCW component accumulates at the boundaries , consistent with the modulation behavior of the TBM without additional coupling. This confirms that NHRE effectively controls mode localization even in the presence of inter-mode coupling.

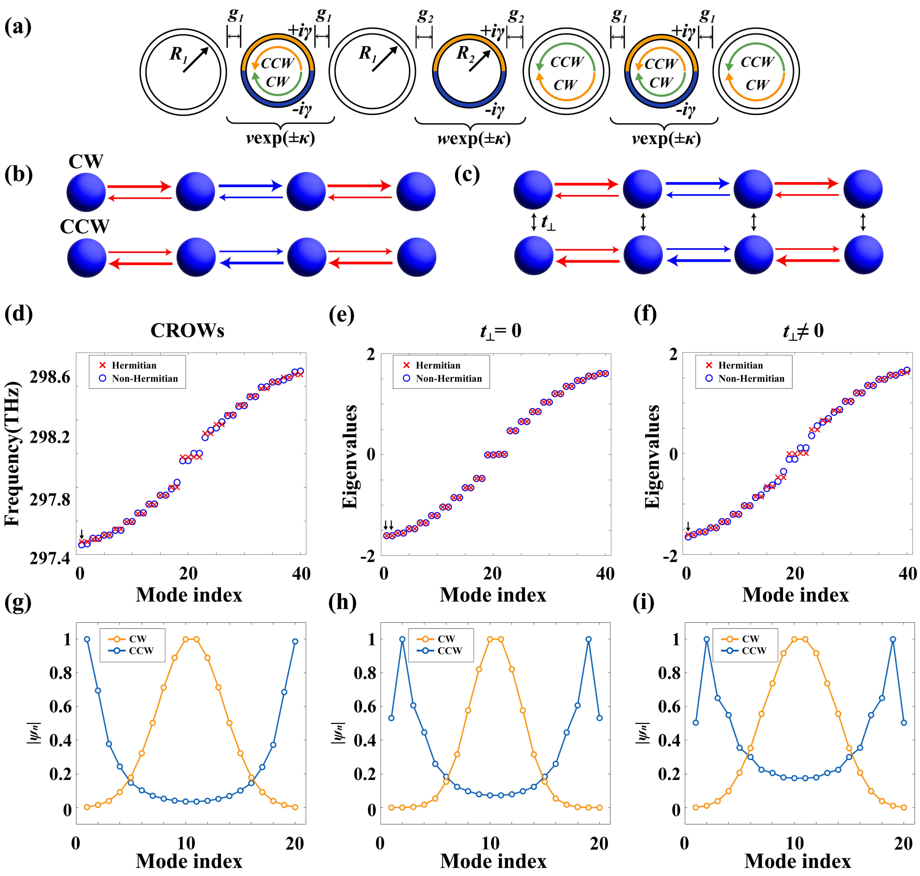

Fig. S7 Verification of NHRE in CROWs. (a) Schematic of the CROW system. (b) Uncoupled and (c) coupled TBM SSH chains. (d–f) Eigenfrequencies of the CROWs and the two TBMs, comparing the Hermitian model (red cross) and the non-Hermitian model (blue circles). (g–i) Projected eigenstates of the non-Hermitian model corresponding to the CW and CCW modes for the eigenstate with the smallest real part of the eigenvalue.